

LA-UR-15-28230 (Accepted Manuscript)

Prediction of MeV electron fluxes throughout the outer radiation belt using multivariate autoregressive models

Sakagushi, K.
Nagatsuma, T.
Reeves, Geoffrey D.
Spence, H. E.

Provided by the author(s) and the Los Alamos National Laboratory (2016-12-02).

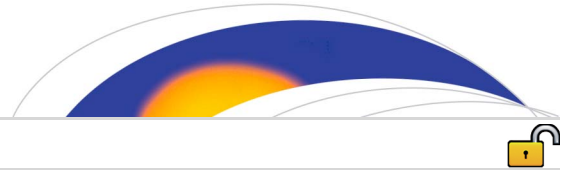
To be published in: Space Weather

DOI to publisher's version: 10.1002/2015SW001254

Permalink to record: <http://permalink.lanl.gov/object/view?what=info:lanl-repo/lareport/LA-UR-15-28230>

Disclaimer:

Approved for public release. Los Alamos National Laboratory, an affirmative action/equal opportunity employer, is operated by the Los Alamos National Security, LLC for the National Nuclear Security Administration of the U.S. Department of Energy under contract DE-AC52-06NA25396. Los Alamos National Laboratory strongly supports academic freedom and a researcher's right to publish; as an institution, however, the Laboratory does not endorse the viewpoint of a publication or guarantee its technical correctness.



RESEARCH ARTICLE

10.1002/2015SW001254

Key Points:

- Prediction models of the outer radiation belt are developed
- The models cover the region of L values from 3 to 6
- The data of 2.3 MeV electron flux from Van Allen Probes mission are used as predictors

Correspondence to:

K. Sakaguchi,
kaoris@nict.go.jp

Citation:

Sakaguchi, K., T. Nagatsuma, G. D. Reeves, and H. E. Spence (2015), Prediction of MeV electron fluxes throughout the outer radiation belt using multivariate autoregressive models, *Space Weather*, 13, 853–867, doi:10.1002/2015SW001254.

Received 26 JUN 2015

Accepted 24 NOV 2015

Accepted article online 26 NOV 2015

Published online 22 DEC 2015

Prediction of MeV electron fluxes throughout the outer radiation belt using multivariate autoregressive models

Kaori Sakaguchi¹, Tsutomu Nagatsuma¹, Geoffrey D. Reeves², and Harlan E. Spence³
¹National Institute of Information and Communications Technology, Koganei, Japan, ²Los Alamos National Laboratory, Los Alamos, New Mexico, USA, ³Institute for the Study of Earth, Oceans, and Space, University of New Hampshire, Durham, New Hampshire, USA

Abstract The Van Allen radiation belts surrounding the Earth are filled with MeV-energy electrons. This region poses ionizing radiation risks for spacecraft that operate within it, including those in geostationary orbit (GEO) and medium Earth orbit. To provide alerts of electron flux enhancements, 16 prediction models of the electron log-flux variation throughout the equatorial outer radiation belt as a function of the McIlwain L parameter were developed using the multivariate autoregressive model and Kalman filter. Measurements of omnidirectional 2.3 MeV electron flux from the Van Allen Probes mission as well as >2 MeV electrons from the GOES 15 spacecraft were used as the predictors. Model explanatory parameters were selected from solar wind parameters, the electron log-flux at GEO, and geomagnetic indices. For the innermost region of the outer radiation belt, the electron flux is best predicted by using the Dst index as the sole input parameter. For the central to outermost regions, at $L \geq 4.8$ and $L \geq 5.6$, the electron flux is predicted most accurately by including also the solar wind velocity and then the dynamic pressure, respectively. The Dst index is the best overall single parameter for predicting at $3 \leq L \leq 6$, while for the GEO flux prediction, the K_p index is better than Dst . A test calculation demonstrates that the model successfully predicts the timing and location of the flux maximum as much as 2 days in advance and that the electron flux decreases faster with time at higher L values, both model features consistent with the actually observed behavior.

1. Introduction

The radiation belts in the Earth's inner magnetosphere are filled with relativistic electrons with energies from hundreds of keV to a few MeV with fluxes that are highly variable. These energetic electrons are trapped by the Earth's magnetic field and bounce/drift around the Earth. Geostationary orbit (GEO; 36,000 km in altitude) is located near the outer boundary of the outer radiation belt. GEO is extremely useful for terrestrial applications, and consequently, numerous satellites for telecommunications, broadcasting, and meteorological purposes densely populate the orbit. The region of space below GEO and above Low Earth orbit (<2000 km in altitude) is called Medium Earth orbit (MEO); MEO satellite passes through the central region of the outer radiation belt and experience energetic particle damage during their passage through the intense electrons in this region. Well-publicized examples of MEO satellites used for navigation include the American Global Positioning System and European Galileo satellites at altitudes near 20,000 km, and the Japanese Quasi-Zenith Satellite System at altitudes of approximately 32,000–39,000 km. The increased use of satellite constellations in MEO as well as GEO results in increased potential risks to instruments and critical satellite systems owing to radiation belt electrons.

Anomalies to instrument or subsystem operations of satellites in the radiation belt result often from an effect known as deep dielectric charging. During such effects, internal electrostatic discharges can impact nearby circuits owing to charge accumulation from energetic electrons that penetrate into dielectric materials after passing through exterior materials of the spacecraft. The typical electron energy range required to produce internal charging is 100 keV to 3 MeV [Garrett and Whittlesey, 2012]. This energy range corresponds to the radiation belt population. An empirical criterion for a spacecraft internal dielectric discharge is an accumulated charge of 10^{10} – 10^{11} electrons per square centimeter over a 10 h period [Ferguson et al., 2011].

Because radiation belt electron flux varies substantially from geomagnetic response to changes in solar wind conditions, spacecraft operators face significant challenges in any countermeasures against the effects of penetrating electrons. These challenges are greatest during geomagnetic storms, when electron fluxes rapidly vary in accordance with changes in the competing loss, transport, and acceleration processes.

©2015. The Authors.

This is an open access article under the terms of the Creative Commons Attribution-NonCommercial-NoDerivs License, which permits use and distribution in any medium, provided the original work is properly cited, the use is non-commercial and no modifications or adaptations are made.

At GEO, the MeV-energy electron flux varies dramatically between 10 and 10^5 ($\text{cm}^{-2} \text{sr}^{-1} \text{s}^{-1}$) over a few days timescale of a typical storm. In such a space environment, satellite ground operators should avoid sending critical commands to satellites that may be facing adverse internal discharging conditions in order to prevent potentially catastrophic consequences to mission operations. Thus, the prediction of radiation belt variations, particularly alerts of any flux enhancement before it reaches a threshold level for charging conditions, is advantageous for ensuring satellite safety.

Many prediction models of the high-energy electron flux at GEO have been proposed, and results from some of these prediction models are readily available via websites. One such early forecast model is the Relativistic Electron Forecast Model (REFM), which is operated by the Space Weather Prediction Center (SWPC) at the National Oceanic and Atmospheric Administration (NOAA). The REFM is based on the work of *Baker et al.* [1990] and uses a linear prediction filter with solar wind speed as an input parameter. In addition, a research group at the University of Colorado developed a means for providing quantitative relativistic electron forecasts by solving the radial diffusion equation using empirical diffusion coefficients as functions of solar wind parameters [Li, 2004]. The model includes the “*Dst* effect” accounting for the adiabatic response of electrons due to changes in the magnetic field. They have also provided forecasts based on the *Turner and Li* [2008] model, called “low-E model,” that is based on a simple source and loss differential equation which takes advantage of a time delay between changes in low- and high-energy electron fluxes. A probabilistic forecast of MeV electrons at GEO has also been provided by the Solar-Terrestrial Environment Laboratory at Nagoya University in Japan. The forecast in their model was established by taking into consideration the solar wind speed as well as the season and sector polarities of the interplanetary magnetic fields [Miyoshi and Kataoka, 2008a]. Furthermore, many additional attempts have been made to forecast high-energy electron flux at GEO using a variety of techniques, including neural network models [Koons and Gorney, 1991; Ling et al., 2010], a data-derived model for daily flux maxima [Ukhorskiy et al., 2004], and a linear prediction using Kalman filters [Rigler et al., 2004]. The Japanese space weather information center at the National Institute of Information and Communications Technology (NICT) [Nagatsuma, 2013] has been providing relativistic electron flux prediction near GEO satellites since 2012 (<http://seg-web.nict.go.jp/radi/en>). Their prediction is based on a multivariate autoregressive (AR) model that calculates future log-flux variations by accounting for a few days lagging response of the electron flux to several solar wind parameter changes [Sakaguchi et al., 2013].

For MEO, the empirical AE-8 and AE-9 trapped electron models without any time dependence are available [Vette, 1991; Ginet et al., 2013]. Because temporal and spatial coverage of observations at MEO are sparse when compared to GEO, empirical approaches are limited. GEO models are more common also because of the many highly valuable satellites at GEO. For nowcasting and forecasting energetic electron fluxes throughout the outer radiation belt, several attempts by physics-based model have been made to calculate the entire flux in the outer radiation belt. *Fok et al.* [2008] developed the Radiation Belt Environment model to provide real-time nowcasting of the outer belt electron flux. The model is based on the bounce-averaged Boltzmann transport equation taking into account the realistic, time-varying magnetic field and considers effects of wave-particle interactions with whistler mode chorus waves. The space environment group at the University of California, Los Angeles, has developed a 1 MeV electron forecast diffusion-based model using the data-assimilative Versatile Electron Radiation Belt (VERB) code [Subbotin et al., 2011] with the forecast boundary flux obtained from the Geosynchronous Radiation-belt Electron Empirical Prediction model. Similarly, *Pakhotin et al.* [2014] coupled the data-driven Nonlinear Autoregressive Moving Average with eXogenous inputs model and the VERB code to simulate the outer radiation belt environment. The SPACECAST project (www.fp7-spacecast.eu) [Horne et al., 2013] has developed two forecasting systems using a diffusion-based formalism which are completely independent: one is the British Antarctic Survey radiation belt model and the other is the Salammbô model developed at the Aerospace Research Laboratory (Office National d’Etudes et de Recherche Aéronautiques), France [Beutier et al., 1995; Varotsou et al., 2005, 2008]. Despite all these efforts at building physics-based predictive models, the dynamic variations throughout the radiation belt in the Sun-Earth system nevertheless remain a substantial challenge for the space physics community. Consequently, empirical approaches are practical and extremely useful, oftentimes providing better and more timely predictions and forecasts than purely physical based numerical simulations.

In September 2012, the Van Allen Probes were launched into the inner magnetosphere to explore the radiation belts in order to understand their dynamical nature. The data from this mission have been acquired since launch for more than 2 years now. This long, continuous time series of data represents a new opportunity for

developing improved empirical prediction models throughout the equatorial radiation belt at $L = 3\text{--}6$ in MEO. For example, the multivariate AR method used for GEO [Sakaguchi *et al.*, 2013] can now be applied to predict flux variations at each L value region in MEO.

In this article, we develop and present new prediction models for MeV electron flux variations throughout the outer radiation belt based on Van Allen Probe measurements made during the maximum of Solar cycle 24. In section 2, the multivariate AR model and Kalman filter are briefly introduced. In section 3, the data set of the predictor and input driver parameters are explained. In section 4, cross-correlation functions between time series of predictor and model driver candidates are shown. In section 5, estimation methods of AR coefficient matrices are described. Lastly, prediction results are validated using skill scores in section 6 and summarized in section 7.

2. Multivariate Autoregressive (AR) Model

The AR model is a representation of a time series in which the current value is modeled as a linear combination of its previous values. The multivariate AR model is a natural extension of the univariate AR model to a multivariate time series vector. The multivariate model is suitable for explaining the interaction among multiple time series, and thus, variations of radiation belt electron flux can be predicted on the basis of its correlation with changes in other conditions. The details of the model are described in a previous paper [Sakaguchi *et al.*, 2013]. The formula for the representation is briefly introduced here.

Let us consider k time series variates $\{y_1(t), \dots, y_k(t)\}$. A multivariate time series at time t is denoted by the $(1 \times k)$ vector $\mathbf{Y}(t) = [y_1(t), \dots, y_k(t)]^T$. A predictor time series is set as y_1 and explanatory (driver input) time series are set as y_2, \dots, y_k . The multivariate AR model with regression order m has the form

$$\mathbf{Y}(t) = \sum_{n=1}^m \mathbf{A}(n)\mathbf{Y}(t-n) + \mathbf{v}, \quad (1)$$

where \mathbf{A} is the $(k \times k)$ coefficient matrix as a function of the regression order and $\mathbf{v} \sim N(\mathbf{0}, \mathbf{W})$ is the $(1 \times k)$ vector of Gaussian white noise, the mean vector and variance-covariance matrix of which are $\mathbf{0}$ and \mathbf{W} , respectively. The coefficient matrix \mathbf{A} is determined by the least squares method using the householder transformation [Akaike *et al.*, 1979]. Here note that the AR model assumes the time series data to be normally distributed around a zero mean. The MeV electron flux closely follows a lognormal distribution. Therefore, the predictor time series consists of the common logarithmic values of the flux and all the observation data are transformed into relative values by subtracting the sample mean of the time series, $\mathbf{Y} = \mathbf{Y} - \langle \mathbf{Y} \rangle$, where $\langle \rangle$ is the sample mean over the past 60 days corresponding to roughly two solar rotations. The AR model can predict the fluctuation component of the electron logarithmic flux, $\Delta \log_{10}(F)$.

The time evolutions of prediction values are estimated using the Kalman filter [Kalman, 1960] approach. A Kalman filter is used to estimate the optimal mean vector and variance-covariance matrix of the current and one-step-ahead states on the basis of the latest observation data. The state space representations of the multivariate AR model and the Kalman filtering and prediction equations are described in Sakaguchi *et al.* [2013].

3. Data Set

3.1. Predictor Time Series

Radiation belt electron flux data observed by the Relativistic Electron and Proton Telescope (REPT) [Baker *et al.*, 2012] of the Radiation Belt Storm Probes Energetic Particle, Composition, and Thermal Plasma Suite (RBSP-ECT) [Spence *et al.*, 2013] on the Van Allen Probe A satellite are used as the predictor time series for modeling. The data obtained by only Probe A are enough because we use 1 day averaged data for the analysis. There is no difference in models, which are generated by Probe A, Probe B, or Probe A + B. The Van Allen Probes were launched in August 2012 with low-inclination angles of about 10° . The apogee and perigee are about $6 R_E$ and 700 km, respectively, and the orbital period is about 9 h. The predictor time series as a function of L values are generated by logarithmic daily-average calculations of omnidirectional electron flux at the energy of 2.3 MeV from the second lowest energy channel of REPT. McIlwain's L values based on the quiet external OP77Q [Olson and Pfizter, 1977] and internal International Geomagnetic Reference Field magnetic field models are used for the determination of the satellite position. The L time diagram of 2 year observation data from September 2012 to August 2014 is shown in Figure 1e. Fifteen daily-average time

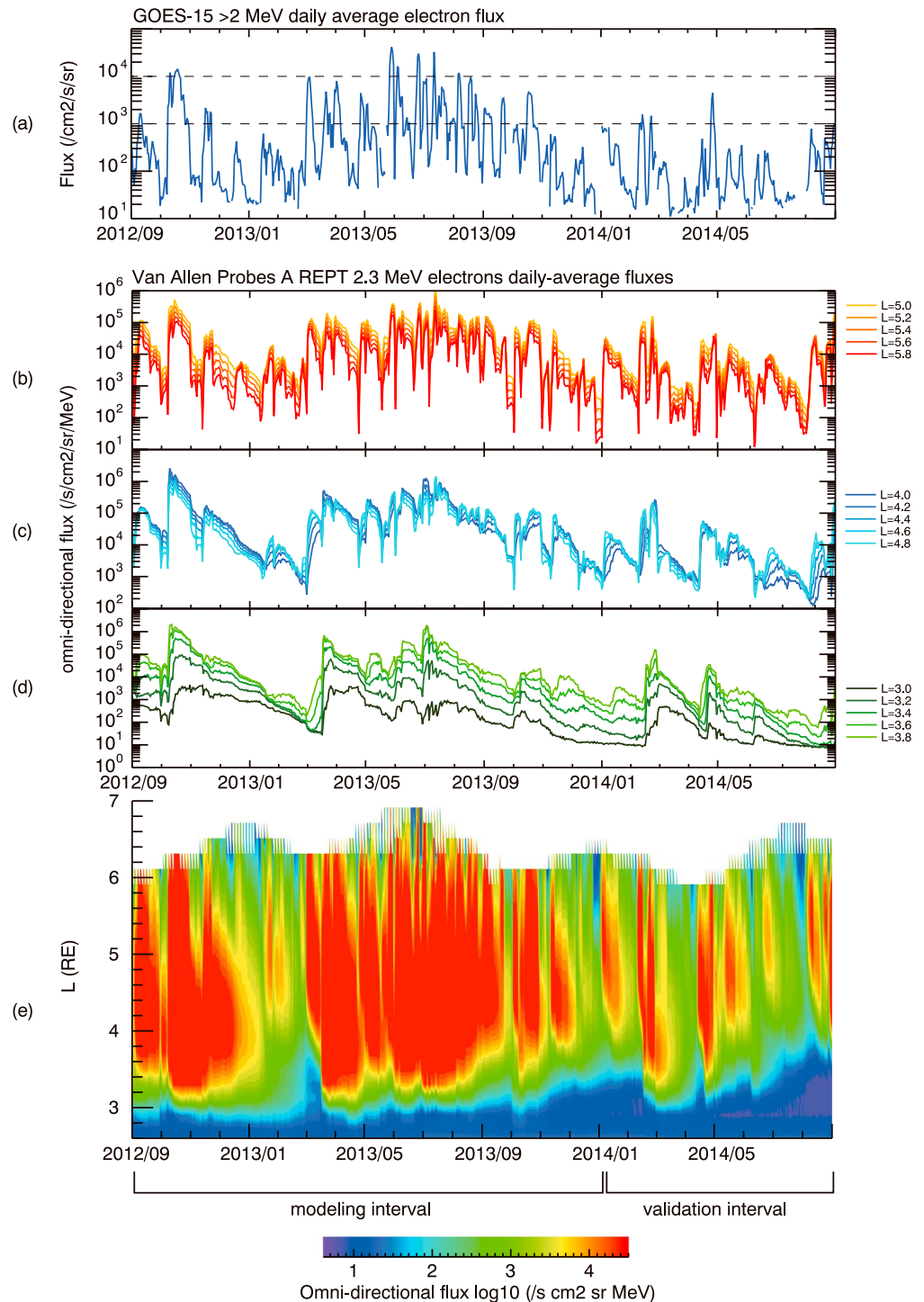


Figure 1. Time series plots and an L time diagram of the daily-average electron fluxes in the outer radiation belt from September 2012 to August 2014. (a) The GOES 15 observation of >2 MeV electrons at GEO. (b–d) The Van Allen Probe A observation of 2.3 MeV electrons at $L = 3$ –6 with $\Delta L = 0.2$. (e) A L time diagram of 2.3 MeV electrons observed by the Van Allen Probes A.

series plots at L values between 3 and 6 with $\Delta L = 0.2$ are shown in Figures 1b–1d. The log values of these time series are used as predictors at MEO. The time series data from September 2012 to December 2013 are used for the training of the models. Data in the remaining interval between January and August 2014 are used for the model validation.

In addition, relativistic electron log-flux data at energies of >2 MeV from the GOES 15 observation are used as a predictor at GEO. Also, the GOES data are used as an explanatory parameter for the prediction of MEO flux variations inside of the GOES location. Figure 1a shows the GOES 15 measurement of daily-average flux variation for the same periods as the Van Allen Probe observations. The two horizontal dashed lines indicate thresholds of electron flux warning levels defined by NICT, from quiet to high and extreme, from bottom to top, respectively.

From the comparison between the time series data plots, it is clear that the characteristics of the variability are different in each region. In particular, the fluctuation period becomes shorter as L increases. The timescale of decay appears longer than that of growth at lower L values. Multivariate AR models are applied to each L value region, and the best combinations of explanatory parameters for each are selected among the solar wind parameters, geomagnetic indices, and GOES measurement data.

3.2. Explanatory Time Series

Geomagnetic indices and solar wind parameters are examined as candidate explanatory time series for modeling. These data are obtained from the OMNI data set. Daily-average time series are generated for the solar wind speed, V_{SW} ; the solar wind dynamic pressure, P_{SW} ; and the north-south component of the solar wind magnetic field, $B_{SW,Z}$, for the same period as the Van Allen Probe observations. These three time series were used as explanatory parameters for the previous GEO prediction model [Sakaguchi *et al.*, 2013]. In addition, five other daily-average time series, namely, the southward component of the solar wind magnetic field, $B_{SW,S}$ ($B_S = -B_Z$ at $B_Z < 0$, $B_S = 0$ at $B_Z > 0$), the geomagnetic indices K_p , Dst , and AE , and the GOES observations of >2 MeV electron log-flux, $\log_{10}(F_{GEO})$, are newly examined in this study. We transform the K_p index values from their native format as stored in the OMNI data set of 0, 0+, 1–, 1, 1+, 2–, ..., in the range from 0 to 9 into a numerically tractable form such that $K_p = 0, 3, 7, 10, 13, 17, \dots$, in the range from 0 to 90. The native K_p index values with plus and minus signs are mapped as 0+ to 3, 1– to 7, 1 to 10, 1+ to 13, 2– to 17, and so on. The daily-average time series (including the transformed version of the K_p index) from September 2012 to December 2013 are plotted in Figure 2.

4. Cross-Correlation Analysis

Firstly, cross-correlation functions between the predictor and the eight explanatory candidates are investigated, as shown in Figure 3. The cross-correlation functions between the radiation belt fluxes, $\log_{10}(F)$ and the solar wind parameters (a) V_{SW} , (b) B_Z , (c) B_S , (d) P_{SW} , and the geomagnetic indices (e) K_p , (f) Dst , (g) AE , and (h) GEO electron flux $\log_{10}(F_{GEO})$ are plotted. The vertical axis is the correlation coefficient and the horizontal axis is the number of lag days. Line colors indicate predictors at different L values: black lines for GEO and red, blue, and green lines for $L = 5-6$, $L = 4-5$, and $L = 3-4$, respectively. All of these cross-correlation functions show that the correlations decrease with decreasing L values. In general, an explanatory time series that shows a high cross correlation to the predictor improves the goodness of the model, and a longer time lag to the cross-correlation peak results in the lead time extension of prediction. Thus, poor cross correlations indicate the greater difficulty of modeling at lower L location than at higher L locations. The detailed interpretation of the cross-correlation relations between the predictor and the explanatory time series are described below.

4.1. Solar Wind Speed: V_{SW}

The solar wind speed is a parameter which is well known to be positively correlated with the relativistic electron log-flux variation at GEO [e.g., Paulikas and Blake, 1979]. In our study, the maximum cross-correlation coefficient is calculated to be 0.57 with $\log_{10}(F_{GEO})$ at the time delay of +2 days, indicating that variations of the radiation belt electron flux at GEO statistically delays 2 days against changes of the solar wind speed. With decreasing L values, the maximum coefficient decreases and the time delay increases; the maximum coefficient (time delay) is calculated to be 0.51 (+2 days) at $L = 5.6$, 0.37 (+3 days) at $L = 4.6$, and 0.18 (+8 days) at $L = 3.6$. This variation in the cross correlation with L values is similar to that in a previous study by Vassiliadis *et al.* [2002].

4.2. Solar Wind Magnetic Field: $B_{Z,SW}$, $B_{S,SW}$

A southward solar wind magnetic field is considered a necessary condition for an increase in the relativistic electron flux as well as a high solar wind speed [Miyoshi and Kataoka, 2008b]. The cross-correlation

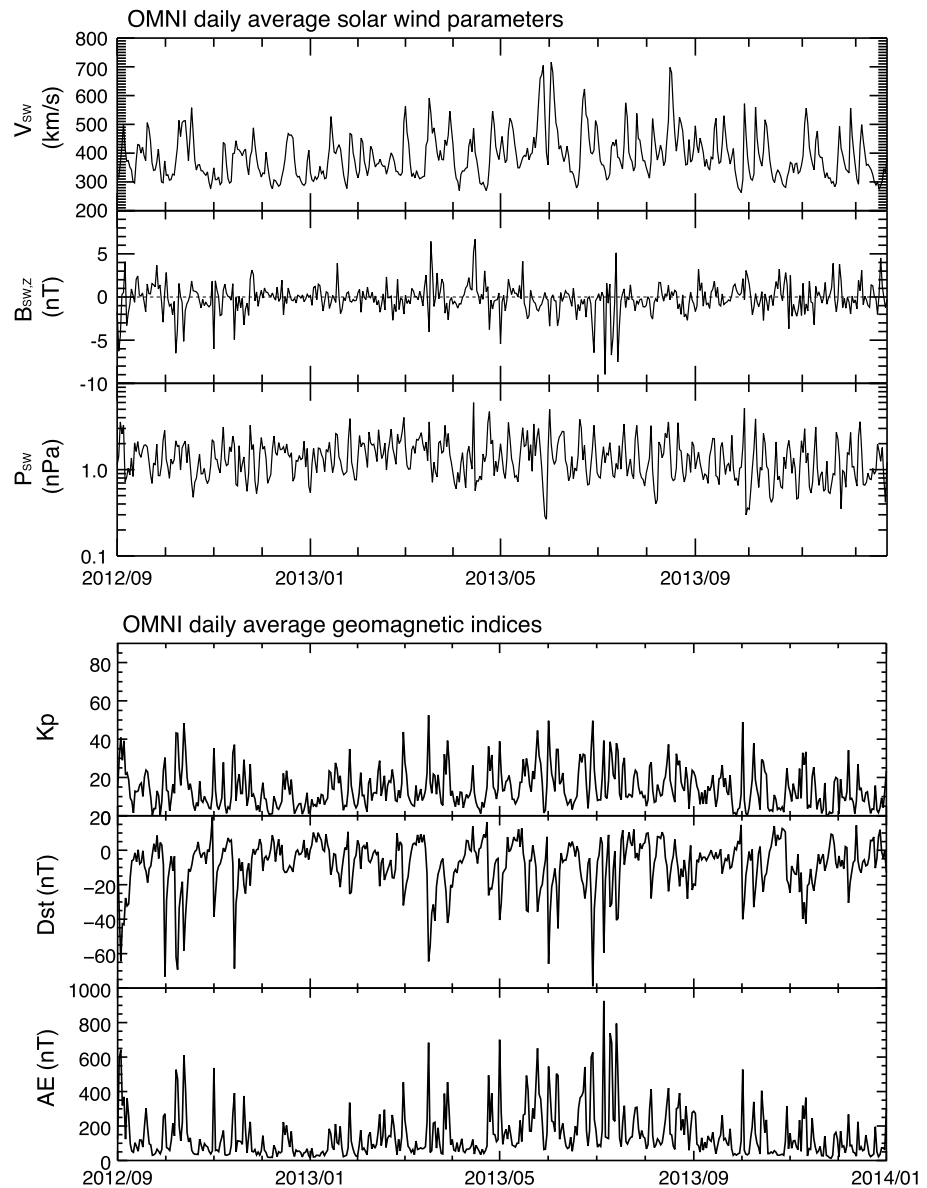


Figure 2. Explanatory time series parameters: (top) solar wind speed V_{SW} , north-south component of magnetic field $B_{SW,Z}$, and pressure P_{SW} and (bottom) geomagnetic indices K_p , Dst , and AE .

functions between the relativistic electron fluxes and $B_{Z,SW}$ show different shapes between GEO and the other L regions. The minimum peak of the cross correlation at GEO is located at a time delay of +3 days, while those at $L < 5.8$ are located at a time delay of +10 days. The negative correlation indicates an increase in the radiation belt electron flux after the change in the magnetic field direction from northward to southward. The minimum value among the peaks is found to be between $\log_{10}(F_{L=4.6})$ and $B_{Z,SW}$ at a delay time of +10 days.

In contrast to the broad shapes of the cross-correlation functions with $B_{Z,SW}$, those with $B_{S,SW}$ show sharp peaks at both negative and positive values. The negative maximum is found between $\log_{10}(F_{L=5.8})$ and B_S at a time delay of ± 0 day, while the positive maximum is found between $\log_{10}(F_{L=5.6})$ and B_S at a time delay of +5 days. The positive peak values of the coefficients are larger than the absolute values of the negative peaks. Such a shape of the function statistically indicates that a small depletion of electron flux occurs just after B_S increases, and then the flux gradually increases for 5 days.

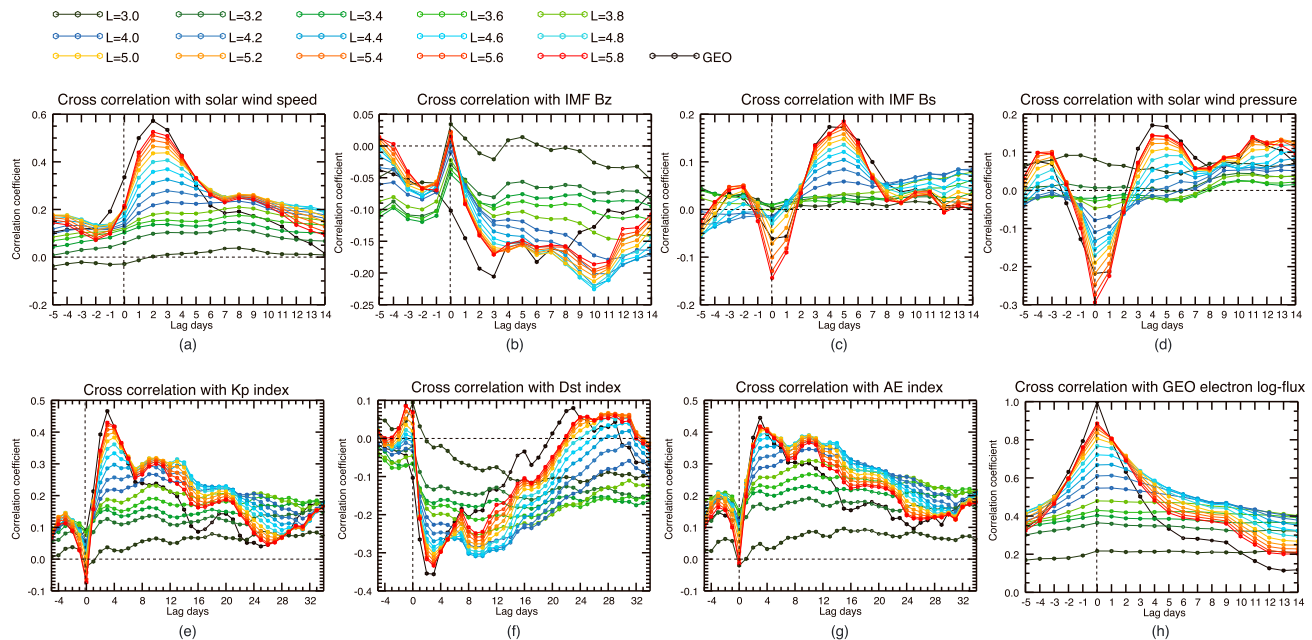


Figure 3. Cross-correlation functions between predictor and explanatory parameters, i.e., radiation belt log-fluxes $\log_{10}(F)$ and solar wind parameters (a) V_{SW} , (b) B_Z , (c) B_S , and (d) P_{SW} and geomagnetic indices (e) K_p , (f) Dst , (g) AE , and (h) GEO electron log-flux $\log_{10}(F_{GEO})$. The vertical axis is the correlation coefficient, and the horizontal axis is the number of lagging days. Line colors indicate the predictors at different L values: black lines for GEO and red, blue, and green lines for $L = 5-6$, $L = 4-5$, and $L = 3-4$, respectively.

4.3. Solar Wind Dynamic Pressure: P_{SW}

The magnetopause shadowing process during solar wind pressure enhancements represents one extremely prompt loss mechanism for relativistic electrons on open drift paths that encounter the magnetopause [e.g., Turner *et al.*, 2012]. Some of the cross-correlation functions between the relativistic electron log-fluxes and the solar wind dynamic pressure in Figure 3d show negative peaks at a time delay of ± 0 day, indicating that the depletion of flux occurs coincidentally with the pressure increase. With increasing L values, negative values of coefficient peaks increase while the peaks become unclear in the cross-correlation functions with electron log-flux at $L < 4$ where the negative peak coefficients are low. This L dependence of cross-correlation relations with solar wind dynamic pressure shows a statistical boundary of loss processes (e.g., magnetopause shadowing) during the analyzed period.

4.4. K_p Index: K_p

K_p index represents the global activity level of the geomagnetic disturbance on the ground at subauroral latitudes. K_p index correlates with the strength of magnetospheric convection [Thomsen, 2004]. The first prediction model of the relativistic electron log-flux at GEO was designed on the basis of daily sums of K_p as input data [Nagai, 1988]. In our study, the maximum cross-correlation coefficient is calculated to be 0.47 with the log-flux at GEO at a time delay of +3 days, indicating that the radiation belt electron log-flux at GEO statistically increases 3 days after K_p increases. The maximum values of the cross-correlation coefficients decrease with decreasing L values, while the corresponding delay times of the correlation peaks become longer; +3 days at $L = 5.6$, +4 days at $L = 4.6$, and +9 days at $L = 4.0$.

4.5. Dst Index: Dst

Dst index represents the global activity level of a geomagnetic storm. The cross-correlation functions between Dst and the relativistic electron log-fluxes show negative correlations in positive lag times. The negative maximum correlation is calculated with the log-flux at GEO at time delays between +2 and +3 days, indicating that the electron flux at GEO statistically increases 2 or 3 days after Dst decreases. For the log-flux at $L = 3.8-5.8$, in the central region of the outer radiation belt, the cross-correlation functions show double negative peaks at time delays of a few days and about 10 days, which is similar to Figure 3e. The negative maximum correlation of the second peak is calculated with the log-flux at $L = 4.6$ at a time delay of +9 days.

4.6. AE Index: AE

AE index represents the geomagnetic disturbance at auroral latitudes. The cross-correlation functions between AE index and the relativistic electron log-flux show a double positive peak at time delays of a few days and about 10 days, which is similar to the correlation functions with K_p and Dst . The maximum value of the first peak is calculated with F_{GEO} at a time delay of +3 days, indicating that the radiation belt electron log-flux at GEO increases 3 days after AE increases. The maximum correlation of the second peaks is calculated with $\log_{10}(F_{L=4.6})$ at a time delay of +10 days.

4.7. Electron Log-Flux at GEO: $\log_{10}(F_{GEO})$

The cross-correlation functions between the relativistic electron log-fluxes at GEO and each of the L value regions show a fairly high correlation at the time delay of ± 0 day. The highest coefficient is calculated to be 0.89 with log-flux at the largest L value of 5.8, which is closest to GEO. With decreasing L values and longer delay times, the correlation coefficient decreases.

5. Coefficient Matrix Estimation

The parameters of a multivariate AR model consist of an AR coefficient matrix and a white noise vector. The dimension of the coefficient matrix corresponds to the number of inputting time series parameters. The number of AR coefficient matrices is proportional to the regression order, m . Increasing the number of parameters (inputting time series parameters and regression orders) in models almost always improves the goodness of fit. However, too many parameters generally result in poor predictive performance because the complexity increases, which is called overfitting. To determine the best set of explanatory parameters and the regression order m of a multivariate AR model, the Akaike Information Criterion (AIC) minimization approach is used as a measure of the relative quality between models [Akaike, 1974]. The AIC minimization method prevents such overfittings of statistical models. The preferred model is determined by the one with the minimum AIC value. The AIC equation is $AIC = -2(\text{maximum log likelihood}) + 2(\text{number of parameters})$. The goodness of the fit is evaluated by the maximum log likelihood and increasing number of parameters increases the penalty. The maximum log likelihood of the AR model is given by $-\frac{N-m_{\max}}{2}(\log 2\pi W_{11} + 1)$ [Akaike et al., 1979]. The parameters in the first component of the k -variate AR model with the regression order m in equation (1) are $k \times m$ AR coefficients and one white noise v . Then, AIC is given by

$$AIC^m = (N - m_{\max})(\log 2\pi W_{11}^m + 1) + 2(k \times m + 1), \quad (2)$$

where N is the number of time series data points which is prepared for the modeling and m_{\max} is the maximum regression order to be examined. The first m_{\max} data points in the time series are not used for the modeling. The AIC for a multivariate AR model is calculated as a function of regression orders. The optimum regression order for a model is the one that gives a minimum AIC value. The optimum explanatory parameters are also estimated by comparisons of minimum AICs among different models.

Next, we use the AIC minimization method to identify the most important explanatory parameters: daily-average MeV electron log-fluxes at $L = 3.0, \dots, 5.8$ and GEO. Figure 4 shows AIC curves of univariate and two-variate AR models as a function of the regression order. The univariate model consists of a predictor parameter only, and no explanatory parameter is used. The two-variate model consists of one predictor parameter and one explanatory parameter: V_{SW} , B_Z , B_S , P_{SW} , K_p , Dst , or AE. When the minimum AIC value of a two-variate model is smaller than that of a univariate model, the explanatory parameter used in the two-variate model is deemed to have effectively increased the accuracy of the prediction. Otherwise the parameter in a two-variate model, which gives larger minimum AIC values than that of a univariate model, is not considered to be an optimal explanatory parameter for the target predictor. In Figure 4, AIC curves for models at (a) GEO ($6.6 R_E$), (b) $L = 5.6$, (c) $L = 4.6$, and (d) $L = 3.6$ are shown. Eight color lines indicate AIC of two-variate models with V_{SW} (red), B_Z (yellow), B_S (light green), P_{SW} (green), K_p (blue), Dst (purple), and AE (pink), respectively. The gray lines indicate AIC of univariate AR models.

We examine AIC variations of AR models for the GEO electron log-flux prediction in Figure 4a. The minimum AIC of the univariate model is calculated with a regression order of 26 days. The model predicts its future variation from a self-recurrence period of approximately 27 days related to the solar rotation cycle. Minimum AIC values of two-variate models with parameters B_Z and B_S have almost the same values

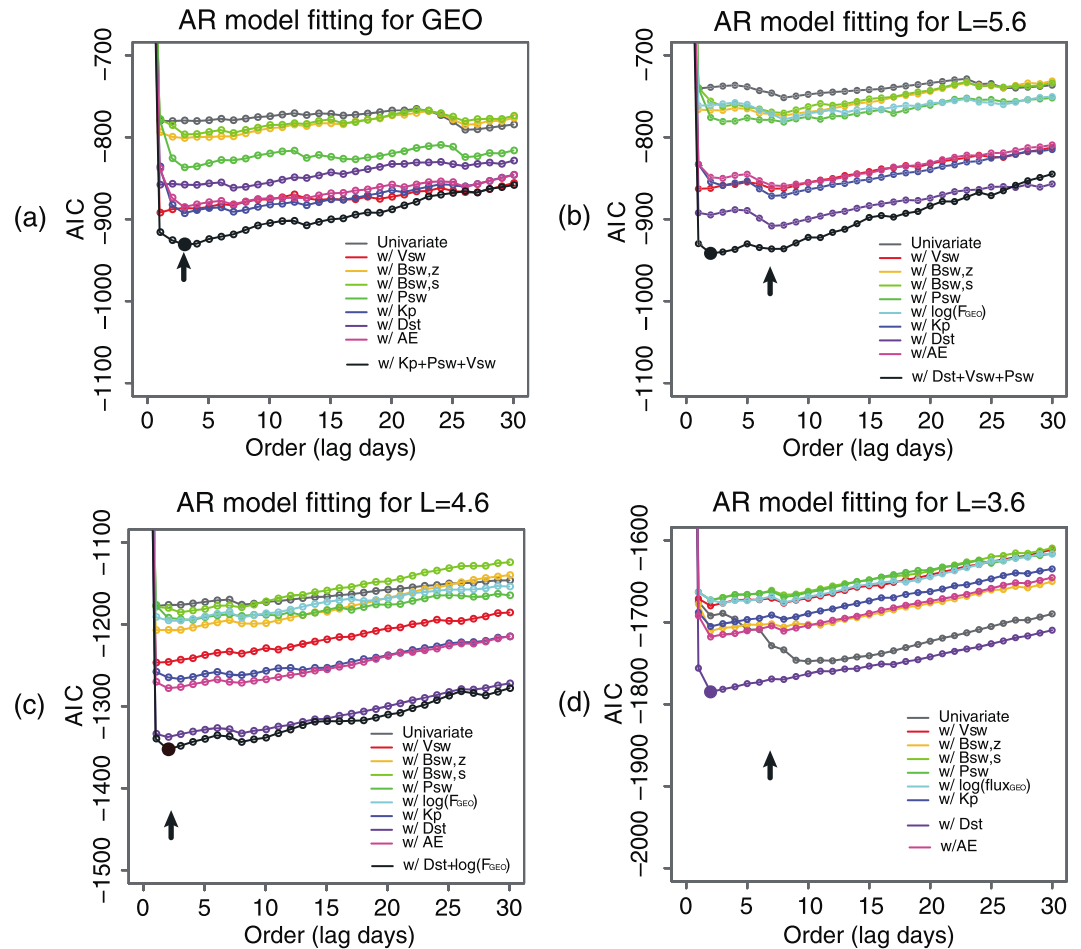


Figure 4. AIC variations of two-variate AR models at (a) GEO ($6.6 R_E$), (b) $L = 5.6$, (c) $L = 4.6$, and (d) $L = 3.6$ as a function of regression order. Eight types of two-variate models are indicated by colored lines: V_{SW} (red), B_z (yellow), B_s (light green), P_{SW} (green), K_p (blue), Dst (purple), and AE (pink). The gray lines indicate AIC variations of univariate AR models. The black lines indicate the estimated final curves, which have the smallest AIC values.

as that of the univariate model, indicating that these are not particularly effective explanatory parameters. Minimum AICs of the other two-variate models are sufficiently smaller than that of the univariate model. In order of minimum AIC from smallest to largest, it is given by two-variate models with a parameter of V_{SW} , K_p , AE , Dst , and P_{SW} in turn. The order corresponds to the order of goodness as the explanatory parameter. Similarly, for the modeling of electron log-flux at $L = 5.6$ shown in Figure 4b, Dst is evaluated as the best explanatory parameters by minimum AIC comparisons. K_p , AE , and V_{SW} are also evaluated to be effective explanatory parameters for improving the model goodness. The remaining two-variate models give minimum AIC values smaller than that of the univariate model, which also possibly improve the prediction performance. The AIC results for $L = 4.6$ shown in Figure 4c is almost the same as that for $L = 5.6$. Lastly, for $L = 3.6$ shown in Figure 4d, Dst is evaluated as the best explanatory parameter; all other parameters are not effective explanatory parameters. Because those minimum AIC values are larger than that of the univariate model, examined parameters except for Dst do not improve the prediction performance at $L = 3.6$.

Second, in order to select the best set of explanatory parameters, AIC curves of multivariate AR models are investigated for all combinations of the explanatory parameters. In Figure 4, the curves, which have the smallest AIC values for $L = 4.6$ and 5.6 and GEO, are plotted as black lines. The optimum set of explanatory parameters and regression order are found to be (V_{SW} , K_p , and P_{SW}) and 3 days for GEO, (V_{SW} , Dst , and P_{SW}) and 2 days for $L = 5.6$, (Dst and $\log(F_{GEO})$) and 2 days for $L = 4.6$, and (Dst) and 2 days for $L = 3.6$, respectively.

Table 1. Summary of Estimated Best Set of Explanatory Parameters for Each L Value and GEO Prediction Models

L Value	Regression Order	Explanation Parameter
$L = 3.0$	5 days	Dst
$L = 3.2$	5 days	Dst
$L = 3.4$	2 days	Dst
$L = 3.6$	2 days	Dst
$L = 3.8$	2 days	Dst
$L = 4.0$	2 days	Dst
$L = 4.2$	2 days	$Dst + \log(F_{GEO})$
$L = 4.4$	2 days	$Dst + \log(F_{GEO})$
$L = 4.6$	2 days	$Dst + \log(F_{GEO})$
$L = 4.8$	2 days	$Dst + V_{SW} + \log(F_{GEO})$
$L = 5.0$	2 days	$Dst + V_{SW} + \log(F_{GEO})$
$L = 5.2$	2 days	$Dst + V_{SW} + \log(F_{GEO})$
$L = 5.4$	8 days	$Dst + V_{SW}$
$L = 5.6$	2 days	$Dst + V_{SW} + P_{SW}$
$L = 5.8$	2 days	$Dst + V_{SW} + P_{SW}$
GEO ($6.6 R_E$)	3 days	$K_p + V_{SW} + P_{SW}$

A summary of the explanatory parameter sets and regression orders that give the minimum AIC is shown in Table 1 for all $L = 3$ –6 and GEO models. The innermost parts of the outer radiation belt at $L = 3.0$ –4.0 are modeled by one explanatory parameter of Dst with regression orders of 5 days for $L = 3.0$ –3.2, and 2 days for $L = 3.6$ –4.0. The central inner parts of the outer radiation belt at $L = 4.2$ –4.6 are modeled by two explanatory parameters, Dst and $\log_{10}(F_{GEO})$ with a regression order of 2 days. The central outer parts of the outer radiation belt at $L = 4.8$ –5.2 are modeled by three explanatory parameters, Dst , V_{SW} ,

and $\log_{10}(F_{GEO})$, with a regression order of 2 days. The electron log-flux at $L = 5.4$ is modeled by two explanatory parameters, Dst and V_{SW} , with a regression order of 8 days. The outer parts of the outer radiation belt at $L = 5.6$ –5.8 are modeled by three explanatory parameters, Dst , V_{SW} , and P_{SW} , with a regression order of 2 days. Lastly, the electron log-flux at GEO is modeled by three explanatory parameters, K_p , V_{SW} , and P_{SW} with a regression order of 2 days.

It is found that only one geomagnetic index is selected as an explanatory parameter for each model. This is because any combination of the indices actually increases the AIC values, indicating directly from the formalism that two or more indices as inputs cause an overfitting condition. Dst index is selected as an explanatory parameter for all models at $L = 3.0$ –5.8 except for the GEO model. In particular, the innermost parts at $L = 3.0$ –4.0 are modeled with Dst index only. AIC analyses indicate that Dst performs best at statistically predicting future log-flux levels for those L values.

The 2 MeV electron log-flux at GEO is selected as an explanatory parameter for the model at $L = 4.2$ –5.2. This is because, for AR models, an explanatory parameter, which shows a higher correlation at positive lag to a predictor, is preferable. That is to say that a high correlation is the necessary condition, but a positive time lag is the sufficient condition for improving the goodness of a prediction model. It is indicated in Figure 3h that the cross correlations between $\log_{10}(F_{GEO})$ and $\log_{10}(F_{L=3.0, \dots, 5.8})$ show higher correlations at larger L values, and correlation peaks shift from 0 to positive lag days with decreasing L values. The $\log_{10}(F_{GEO})$ parameter shows correlation peaks at between 0 and +1 lag days for the log-fluxes at $L = 4.2$ –5.2.

The V_{SW} parameter is selected as an explanatory parameter for the models at $L \geq 4.8$. The correlations (shown in Figure 3a) are sufficiently high at positive lag times. There is an evident boundary for V_{SW} as an explanatory parameter at $L = 4.8$. This might be related to some physical processes, such as the inner edge of particle acceleration by ULF waves, a role of inward radial diffusion to lower L shells, the average location of the plasmopause and the role of local acceleration by electrons interacting with whistler mode chorus outside of the plasmasphere. ULF wave activity is known to be mostly related to V_{SW} , while the other conditions are related not only to V_{SW} but also to $B_{SW,Z}$ which is a driver of magnetospheric convection. The P_{SW} parameter is selected as an explanatory parameter for the models at $L \geq 5.6$. The boundary of P_{SW} at $L = 5.6$ also seems to be related to a physical process, perhaps in this case to MeV electron loss owing to magnetopause shadowing. The limit at $L = 5.6$ probably corresponds to a statistical threshold of electron losses due to magnetopause shadowing during the analyzed period from September 2012 to December 2013.

Lastly, and only for the model at GEO, K_p is selected as an explanatory parameter instead of Dst . K_p index includes the middle to higher latitudes geomagnetic activity, such as a substorm activity, whereas the Dst index is dominated by low-latitude geomagnetic disturbances caused in the inner magnetosphere by the storm time ring current. In this study, it is found that the log-flux variations in the main body

of the outer radiation belt are predicted well by Dst , while that at GEO, at the outer edge of the radiation belt, is predicted well by K_p . This is probably because Dst index corresponds to lower L value disturbance and K_p corresponds to middle/higher L value one by considering the latitudes of the contributing ground stations. This may contribute to K_p working better for higher L value than Dst . In addition, this may be due to the L dependence of typical electron flux variations. For example, the K_p index increases when the global convection field increases [Thomsen, 2004], which in turn transports energetic particles into the inner magnetosphere from the plasma sheet. On the other hand, the difference may also result from the difference of energy ranges (and flux units) between observations made in MEO and GEO in our study.

In a previous study [Sakaguchi et al., 2013], B_z was used as an explanatory parameter of the GEO flux modeling because electron enhancements by both the seed electron transport and the acceleration by whistler waves generally occur during a southward solar wind magnetic field condition. However, our present study suggests that the flux of radiation belt electrons varies in relation to geomagnetic disturbances rather than the magnetic field strength of the upstream solar wind. As an outcome of our work, the radiation belt electron flux forecast model of NICT for GEO will soon be updated and improved from the initial B_z -based model to a newly demonstrated K_p -based model.

6. Prediction Results and Validation

The time evolutions of MeV electron log-flux variation at each L value are calculated using a Kalman filter. Figure 5 shows the predicted time series of electron flux (red line) for approximately 240 days from 1 January 2014, which is after the interval used for the modeling. Lead time of prediction is 1 day, which means one-step-ahead predictions. Pink lines at the top and bottom of the predicted values indicate the margin for 1 sigma error, a standard deviation. Black dots indicate the actual observation values by the Van Allen Probe A. The observation and prediction at (a) GEO, (b) $L=5.6$, (c) $L=4.6$, and (d) $L=3.6$ are overplotted in each panel. Almost all the observation values are located within the margin of the prediction error. Some of the observation values are located outside of the error margin. The blue and green lines indicate the differences in overestimations and underestimations outside of the error margin, respectively. Prediction failures are mostly found during periods of rapid increase or decrease, such as around days 40 and 60. This could be from insufficient time resolution (1 day average) for predicting rapid evolution, or it may also be due to the lack of explanatory parameters for a particular type of change. If such a change results from nonlinear evolution, a linear statistical model cannot correctly predict the nonlinear effect owing to its very construction.

Figure 6 shows an example of long-term prediction over 10 days. The predictions more than one-step ahead (n step) can be computed by n times iterations of the one-step prediction equation without filtering steps. Details of n -step prediction methods are described in Sakaguchi et al. [2013]. The prediction calculation shown in Figure 6 was done on the 131st day of year 2014, during a time of electron flux enhancements. Observation data before 131 days are used for Kalman filtering calculations. Figure 6 (left) shows an L time diagram for 2.3 MeV electron flux observed by the Van Allen Probe A. Figure 6 (right) shows long-term predictions; fluxes at days +1, +2, ..., +10 correspond to 1, 2, ..., 10 day ahead predictions. Data at the day numbers of less than 0 are observations used as inputs for filtering calculations. The Kalman prediction successfully reproduces that the outer radiation belt electron flux maximizes at day +2 at $L=4.6$ –5.0. The long-term forecast can also predict that after the maximum the flux decreases with a higher decay rate at higher L values, consistent with the actual observation.

The prediction results for 240 days in 2014 shown in Figure 5 are evaluated using two skill scores, which are introduced in the website of NOAA/SWPC (legacy-www.swpc.noaa.gov/refm/doc/REFMDoc.html). The skill score is a relative measure of prediction performance between the target and a reference forecast. It evaluates whether the AR model performs better or worse than some reference models. The equation of the skill score (SS) is given by $SS = \frac{MSE_{\text{reference forecast}} - MSE_{\text{target forecast}}}{MSE_{\text{reference forecast}}}$, where MSE is a mean square error, $MSE = \frac{1}{N} \sum (\text{observed} - \text{forecast})^2$. For MSE calculations, we used different two reference forecasts, one is a sample mean value and the other is the most recent observation. The skill score based on a sample mean value is called "prediction efficiency" and that based on the most recent observation is called "persistence SS." The persistence forecast assumes that the conditions at the time of the forecast will not change

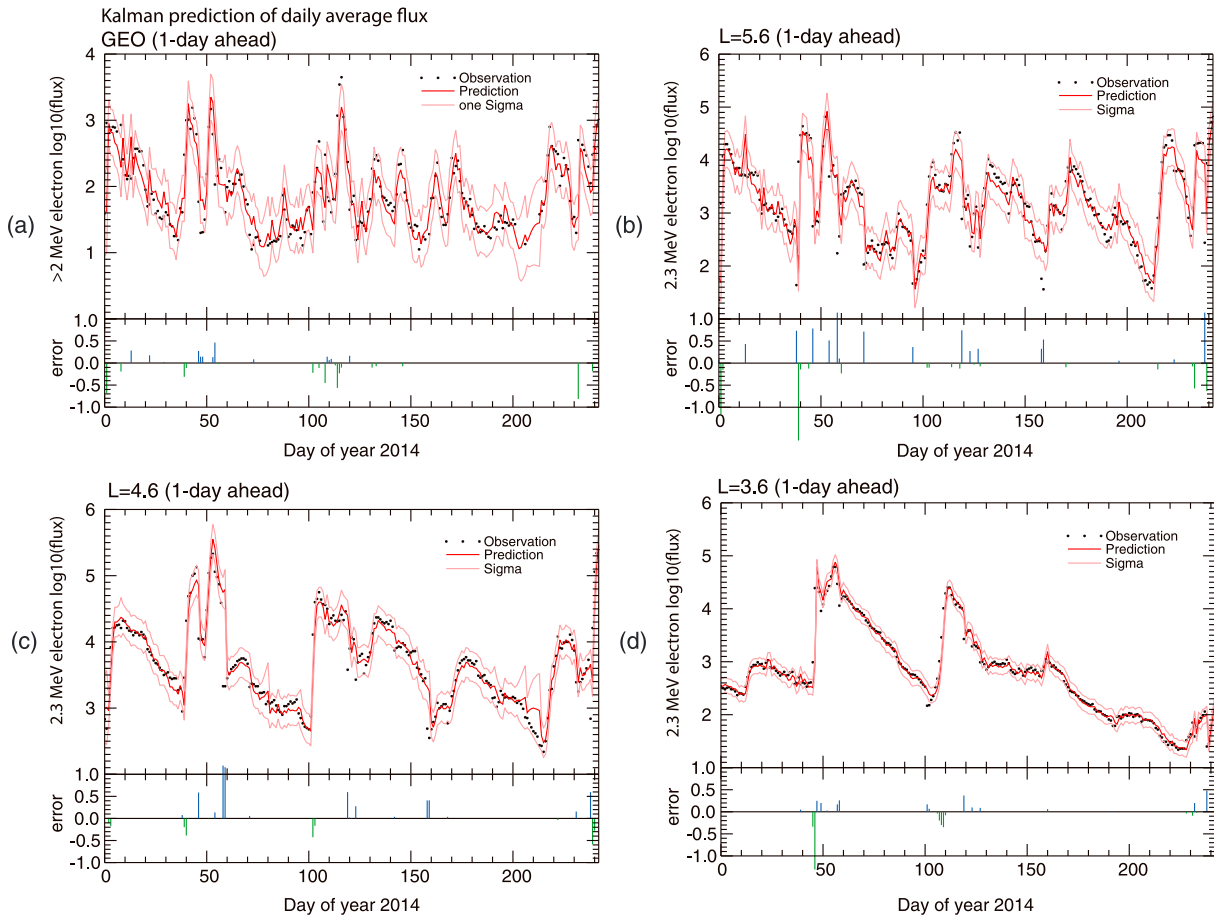


Figure 5. Comparisons of daily-average fluxes between 1 day ahead prediction (red line) and actual observation by the Van Allen Probe (black dots) at (a) GEO, (b) $L = 5.6$, (c) $L = 4.6$, and (d) $L = 3.6$ for 240 days from 1 January 1. Pink lines above and below the predicted values indicate the margin of 1 sigma error. The blue and green lines indicate the difference in overestimations and underestimations outside of the error margin, respectively.

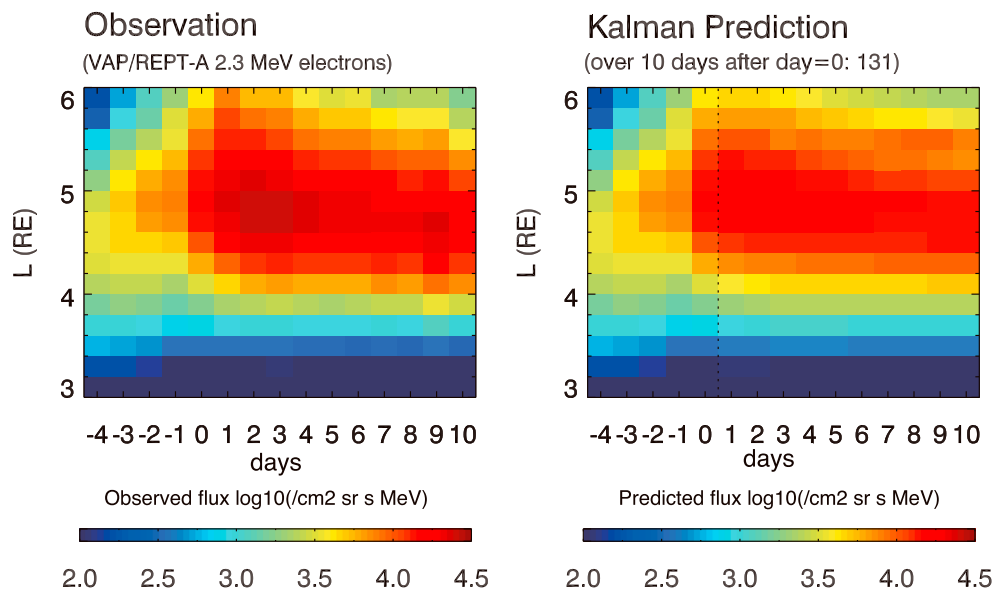


Figure 6. Example of a long-term prediction over 9 days after day of year 131 in 2014. (left) An L time diagram for 2.3 MeV electron daily-average log-flux observed by the Van Allen Probe A. (right) A long-term prediction. Data at the day numbers of less than 0 are the observation values used as inputs for filtering calculations.

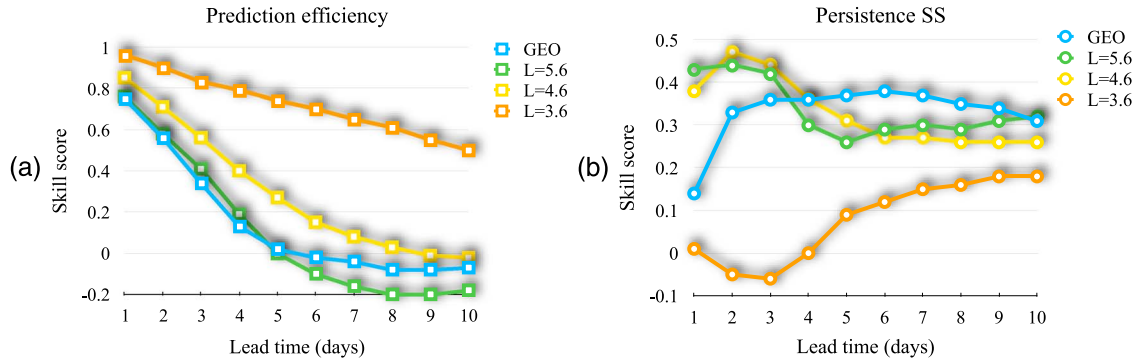


Figure 7. Prediction validations by skill scores: (a) PE and (b) Persistence SS for 240 days in 2014 as a function of prediction lead time.

and that future weather will be the same as the present. The prediction efficiency is calculated by inputting a sample mean of the observation as a reference forecast:

$$\text{Prediction efficiency} = 1 - \frac{\sum_i (y_i - p_i)^2}{\sum_i (y_i - \bar{y})^2}. \quad (3)$$

Persistence SS is calculated by inputting the present observation value at the time of the forecast as a reference forecast:

$$\text{Persistence SS} = 1 - \frac{\sum_i (y_i - p_i)^2}{\sum_i (y_i - y_{\text{latest}})^2}, \quad (4)$$

where y_i is the logarithmic value of the observed relativistic electron flux at time i and p_i is that of the forecast value. The skill score ranges from +1.0 (perfectly correct) to $-\infty$ (not correct); positive and negative values, respectively, indicate better and worse performances than the reference forecast. Figure 7 shows the (a) prediction efficiency (PE) and (b) Persistence SS of prediction results for 240 days in 2014 as a function of the prediction lead time.

The skill score of PE becomes +1 as the prediction error variance approaches zero, and conversely, the score becomes negative when the error variance is larger than the observation variance. Figure 7a shows that the skill score of PE decreases as the lead time becomes longer. The denominator of the second term of PE is the variance of observation values, while the numerator is the variance of the prediction error. For GEO and $L = 5.6$, the scores are computed to be less than 0 after a lead time of 5 days. For $L = 4.6$, the score becomes less than 0 after a lead time of 9 days. In terms of the PE examination, the forecast is evaluated as being useful up to a lead time of 4 days for $L \geq 5.6$ and a lead time of 8 days for $5.6 > L \geq 4.6$.

The Persistence SS is calculated by inputting current observation values into the denominator of the second term as the reference forecast, which indicates that today's condition continues into the future. This is the simplest prediction method, and it is suitable as a reference forecast for the validation. The Persistence SS are greater than 0 for all L value models with lead times of 1 to 10 days except for $L = 3$ at lead times of 1 to 3 days. This indicates that the AR predictions are valid in highly variable high L regions. On the other hand, at $L = 3$, Persistence SS at shorter lead times are poor since the MeV electron flux varies slowly.

7. Summary

Prediction models of the MeV electron flux variation in the equatorial outer radiation belt at $L = 3-6$ as well as GEO are generated by the multivariate AR method. The daily-average flux of omnidirectional 2.3 MeV electrons from September 2012 to December 2013 obtained by the REPT on board the Van Allen Probe A is used for the predictor time series at MEO along with GOES 15 data of >2 MeV electrons at GEO. Sixteen multivariate AR models are generated for each McIlwain L value between 3 and 6 ($\Delta L = 0.2$) and GEO. The AIC minimization procedure, which prevents overfitting, is used for the selection of explanatory parameters and regression orders. Explanatory parameters are selected among four solar wind parameters (V_{SW} , P_{SW} , $B_{\text{SW},Z}$, and $B_{\text{SW},S}$), three geomagnetic indices (AE , Dst , and K_p), and GEO electron flux ($\log_{10}(F_{\text{GEO}})$). The middle to

inner parts of the outer radiation belt are modeled best with the Dst index (storm activity), while its outer edge is modeled best with the K_p index (substorm activity). The GEO log-flux is selected as an explanatory parameter for electron log-flux modeling at $4.2 \leq L \leq 5.2$. The solar wind pressure and speed are selected for the modeling at $L \geq 5.6$ and $L \geq 4.8$, respectively. The best combinations of explanatory time series and the regression orders are summarized in Table 1. In this study, it is found that K_p is a better explanatory parameter than B_{SWZ} for the modeling of electron flux at GEO. The NICT prediction model will be updated so as to use K_p as an input instead of B_{SWZ} .

The prediction results computed with the current model are validated on the basis of a 240 day data set observed in 2014. Almost all the observation values are located within the margin of the prediction error computed 1 day earlier. The prediction skill scores as a function of lead time are plotted in Figure 7. An example of long-term prediction demonstrates that the model can predict the timing and location of the electron flux maximum 2 days earlier and the decay rate after the maximum.

For real-time operation of the MeV electron flux prediction using the multivariate AR model, current values of electron fluxes at GEO and MEO as well as those of explanatory time series are needed as inputs to the Kalman filtering calculation. The quasi-real-time GEO flux ($\log_{10}(F_{GEO})$) and the explanatory time series data (Dst , K_p , V_{SW} , and P_{SW}) are available. The next Japanese satellite Exploration of Energization and Radiation in Geospace (ERG) mission [Miyoshi *et al.*, 2012] plans to provide real-time observation data of the outer radiation belt electrons in MEO for space weather users. The ERG satellite will be launched in the summer of 2016. After the launch of the ERG satellite, real-time prediction of the MeV electron flux throughout the outer radiation belt will be provided from the Japanese space weather information center of NICT.

Acknowledgments

The authors thank the RBSP-ECT team for providing the REPT data, which are supported by RBSP-ECT funding provided by JHU/APL contract 967399 under NASA's Prime contract NASS-01072. The solar wind parameters and geomagnetic indices are provided from the OMNIWeb Plus (<http://omniweb.gsfc.nasa.gov>) at the Space Physics Data Facility, Goddard Space Flight Center. We thank the World Data Center for Geomagnetism, Kyoto, operated by Data Analysis Center for Geomagnetism and Space Magnetism at Kyoto University, for providing Dst and AE indices. We thank the GFZ German Research Centre for Geosciences for providing K_p indices. We also thank the Space Weather Prediction Center, NOAA, for providing the GOES satellite data.

References

- Akaike, H. (1974), A new look at the statistical model identification, *IEEE Trans. Autom. Control*, 19(6), 716–723, doi:10.1109/TAC.1974.1100705.
- Akaike, H., G. Kitagawa, E. Arahata, and F. Tada (1979), *Computer Science Monograph, No.11, Timsac78*, Inst. of Stat. Math, Tokyo, Japan.
- Baker, D. N., R. L. McPherron, T. E. Cayton, and R. W. Klebesadel (1990), Linear prediction filter analysis of relativistic electron properties at 6.6 R_E , *J. Geophys. Res.*, 95, 15,133–15,140.
- Baker, D. N., et al. (2012), The Relativistic Electron-Proton Telescope (REPT) instrument on board the Radiation Belt Storm Probes (RBSP) spacecraft: Characterization of Earth's radiation belt high-energy particle populations, *Space Sci. Rev.*, doi:10.1007/s11214-012-9950-9.
- Beutier, T., D. Boscher, and M. France (1995), SALAMMBO: A three-dimensional simulation of the proton radiation belt, *J. Geophys. Res.*, 100(A9), 17,181–17,188, doi:10.1029/94JA02728.
- Ferguson, D. C., W. F. Denig, and J. V. Rodriguez (2011), Plasma conditions during the Galaxy 15 anomaly and the possibility of ESD from subsurface charging, paper AIAA#2011-1061 presented at 49th AIAA Aerospace Sciences Meeting, Jan. 4–7.
- Fok, M.-C., R. B. Horne, N. P. Meredith, and S. A. Glauert (2008), Radiation Belt Environment model: Application to space weather nowcasting, *J. Geophys. Res.*, 113, A03S08, doi:10.1029/2007JA012558.
- Garrett, H. B., and A. C. Whittlesey (2012), *Guide to Mitigating Spacecraft Charging Effects*, 194 pp., Wiley, Hoboken, N. J.
- Ginet, G. P., et al. (2013), AE9, AP9 and SPM: New models for specifying the trapped energetic particle and space plasma environment, *Space Sci. Rev.*, 179, 579–615, doi:10.1007/s11214-013-9964-y.
- Horne, R. B., S. A. Glauert, N. P. Meredith, D. Boscher, V. Maget, D. Heynderickx, and D. Pitchford (2013), Space weather impacts on satellites and forecasting the Earth's electron radiation belts with SPACECAST, *Space Weather*, 11, 169–186, doi:10.1002/swe.20023.
- Kalman, R. E. (1960), A new approach to linear filtering and prediction problems, *J. Basic Eng.*, 82, 35–45.
- Koons, H. C., and D. J. Gorney (1991), A neural network model of the relativistic electron flux at geosynchronous orbit, *J. Geophys. Res.*, 96, 5549–5556.
- Li, X. (2004), Variations of 0.7–6.0 MeV electrons at geosynchronous orbit as a function of solar wind, *Space Weather*, 2, S03006, doi:10.1029/2003SW000017.
- Ling, A. G., G. P. Ginet, R. V. Hilmer, and K. L. Perry (2010), A neural network-based geosynchronous relativistic electron flux forecasting model, *Space Weather*, 8, S09003, doi:10.1029/2010SW000576.
- Miyoshi, Y., and R. Kataoka (2008a), Probabilistic space weather forecast of the relativistic electron flux enhancement at geosynchronous orbit, *J. Atmos. Sol. Terr. Phys.*, 70, 475–481.
- Miyoshi, Y., and R. Kataoka (2008b), Flux enhancement of the outer radiation belt electrons after the arrival of stream interaction regions, *J. Geophys. Res.*, 113, A03S09, doi:10.1029/2007JA012506.
- Miyoshi, Y., et al. (2012), The Energization and Radiation in Geospace (ERG) project, in *Dynamics of the Earth's Radiation Belts and Inner Magnetosphere*, edited by D. Summers, et al., pp. 103–116, AGU, Washington, D. C., doi:10.1029/2012GM001304.
- Nagai, T. (1988), "Space weather forecast": Prediction of relativistic electron intensity at synchronous orbit, *Geophys. Res. Lett.*, 15, 425–428, doi:10.1029/GL015i005p00425.
- Nagatsuma, T. (2013), New ages of operational space weather forecast in Japan, *Space Weather*, 11, 207–210, doi:10.1002/swe.20050.
- Olson, W. P., and K. A. Pfizter (1977), Magnetospheric magnetic field modeling, Annual Scientific Report, 96 pp., Air Force Off. of Sci. Res. Contract F44620-75-C-0033, McDonnell Douglas Astronaut. Co., Huntington Beach, Calif.
- Pakhotin, I. P., A. Y. Drozdov, Y. Y. Shprits, R. J. Boynton, D. A. Subbotin, and M. A. Balikhin (2014), Simulation of high-energy radiation belt electron fluxes using NARMAX-VERB coupled codes, *J. Geophys. Res. Space Physics*, 119, 8073–8086, doi:10.1002/2014JA020238.
- Paulikas, G. A., and J. B. Blake (1979), Effects of the solar wind on magnetospheric dynamics: Energetic electrons at the synchronous orbit, in *Quantitative Modeling of Magnetospheric Processes*, edited by W. P. Olson, pp. 180–202, AGU, Washington, D. C.
- Rigler, E. J., D. N. Baker, R. S. Weigel, D. Vassiliadis, and A. J. Klimas (2004), Adaptive linear prediction of radiation belt electrons using the Kalman filter, *Space Weather*, 2, S03003, doi:10.1029/2003SW000036.

- Sakaguchi, K., Y. Miyoshi, S. Saito, T. Nagatsuma, K. Seki, and K. T. Murata (2013), Relativistic electron flux forecast at geostationary orbit using Kalman filter based on multivariate autoregressive model, *Space Weather*, *11*, 79–89, doi:10.1002/swe.20020.
- Spence, H. E., et al. (2013), Science goals and overview of the Energetic Particle, Composition, and Thermal Plasma (ECT) Suite on NASA's Radiation Belt Storm Probes (RBSP) Mission, *Space Sci. Rev.*, doi:10.1007/s11214-013-0007-5.
- Subbotin, D. A., Y. Y. Shprits, and B. Ni (2011), Long-term radiation belt simulation with the VERB 3-D code: Comparison with CRRES observations, *J. Geophys. Res.*, *116*, A12210, doi:10.1029/2011JA017019.
- Thomsen, M. F. (2004), Why K_p is such a good measure of magnetospheric convection, *Space Weather*, *2*, S11004, doi:10.1029/2004SW000089.
- Turner, D. L., and X. Li (2008), Quantitative forecast of relativistic electron flux at geosynchronous orbit based on low-energy electron flux, *Space Weather*, *6*, S05005, doi:10.1029/2007SW000354.
- Turner, D. L., Y. Y. Shprits, M. Hartinger, and V. Angelopoulos (2012), Explaining sudden losses of outer radiation belt electrons during geomagnetic storms, *Nat. Phys.*, *8*, 208–212, doi:10.1038/nphys2185.
- Ukhorskiy, A. Y., M. I. Sitnov, A. S. Sharma, B. J. Anderson, S. Ohtani, and A. T. Y. Lui (2004), Data-derived forecasting model for relativistic electron intensity at geosynchronous orbit, *Geophys. Res. Lett.*, *31*, L09806, doi:10.1029/2004GL019616.
- Varotsou, A., D. Boscher, S. Bourdarie, R. B. Horne, S. A. Glauert, and N. P. Meredith (2005), Simulation of the outer radiation belt electrons near geosynchronous orbit including both radial diffusion and resonant interaction with Whistler-mode chorus waves, *Geophys. Res. Lett.*, *32*, L19106, doi:10.1029/2005GL023282.
- Varotsou, A., D. Boscher, S. Bourdarie, R. B. Horne, N. P. Meredith, S. A. Glauert, and R. H. Friedel (2008), Three-dimensional test simulations of the outer radiation belt electron dynamics including electron-chorus resonant interactions, *J. Geophys. Res.*, *113*, A12212, doi:10.1029/2007JA012862.
- Vassiliadis, D., A. J. Klimas, S. G. Kanekal, D. N. Baker, and R. S. Weigel (2002), Long-term-average, solar cycle, and seasonal response of magnetospheric energetic electrons to the solar wind speed, *J. Geophys. Res.*, *107*(A11), 1383, doi:10.1029/2001JA000506.
- Vette, J. (1991), The AE-8 trapped electron model environment, Rep. 91–24, Natl. Space Sci. Data Cent., Greenbelt, Md.